Applied Energy 306 (2022) 118086

Contents lists available at ScienceDirect

Applied Energy

journal homepage: www.elsevier.com/locate/apenergy

Single photon Lidar gas imagers for practical and widespread continuous methane monitoring

James Titchener *, Doug Millington-Smith, Chris Goldsack, George Harrison, Alexander Dunning, Xiao Ai *, Murray Reed

QLM Technology Ltd, Unit DX, Albert Rd, Bristol BS2 0XJ, United Kingdom

HIGHLIGHTS

- A novel gas imager using Single-Photon Lidar with Tunable Diode Laser Spectroscopy.
- Imaging of methane leaks as low as 0.012 g/s and at ranges of up to 90 m.
- A low power lidar imager for industrial methane monitoring.

GRAPHICAL ABSTRACT

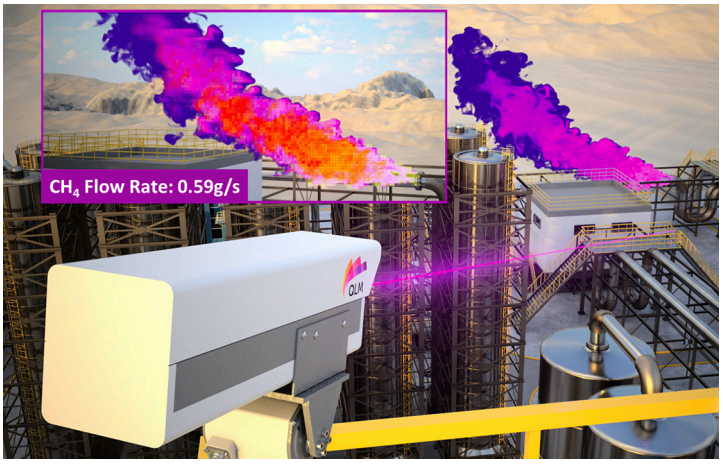

ARTICLE INFO

Keywords:
Natural gas
Methane
Fugitive emissions
Gas sensor
Optical gas imaging
Tunable diode laser absorption spectroscopy

ABSTRACT

The accurate and comprehensive identification and quantification of greenhouse gas (GHG) emissions is an essential part of the management and mitigation of climate change. We are developing a novel remote gas imaging sensor for the detection, visualisation, and quantification of methane emissions. The sensor uses a new technique we call Tunable Diode Lidar (TDLidar) which combines aspects of Tunable Diode Laser Absorption Spectroscopy (TDLAS) with Differential Absorption Lidar (DIAL) and Time Correlated Single Photon Counting (TCSPC) to enable remote spectroscopy and ranging with low power semiconductor diode lasers. Our first TDLidar methane sensors use diode lasers with wavelengths around the CH_4 absorption line at 1.6509 μm and Peltier-cooled Single Photon Avalanche Diode (SPAD) detectors in a Random Modulation Continuous Wave (RM-CW) Lidar system. Here we characterise our TDLidar methane sensor performance with calibrated gas cells and controlled gas release trials and we demonstrate quantification of leak rates as low as 0.012 g/s and detection at distances over 90 m. The accuracy, speed, and practicality of the sensor, combined with an expectation of low-

* Corresponding author.
E-mail addresses: james.titchener@qlmtec.com (J. Titchener), xiao.ai@qlmtec.com (X. Ai).

https://doi.org/10.1016/j.apenergy.2021.118086
Received 1 February 2021; Received in revised form 12 October 2021; Accepted 17 October 2021
Available online 31 October 2021

cost in volume, offers the potential that these sensors can be effectively applied for widespread continuous and autonomous monitoring of industrial methane emissions.

1. Introduction

Methane (CH_4), the main component of natural gas, is the second largest contributor to climate change and has a 20-year global warming potential of 84 times that of carbon dioxide (CO_2) [1,2]. Because CH_4 has a short lifetime in the atmosphere [3], reduction in CH_4 emissions can have a rapid effect on climate forcing. Thus, reducing CH_4 emissions has been identified as a key goal for reducing global warming [4].

One source of anthropogenic CH_4 emissions is the oil and gas sector [5,6,7]. There are over 500,000 active gas well pads in the U.S.A alone, and many industrial sites. Measurement campaigns have shown that many sites are leaking much more than expected. For example up to 3.7 % of CH_4 gas extracted from the Permian basin is emitted into the atmosphere, which is over 60 % more than initial emissions studies predicted [8].

Major companies within the energy industry have made commitments towards CH_4 emissions monitoring and reduction in compliance with, and often ahead of, expanding government regulations. To this end there is a push to develop affordable and practical ways of implementing leak detection and repair (LDAR) operations across the industry. CH_4 emissions in the oil and gas industry follow a highly skewed distribution, where a small number of sites contribute the vast majority of emissions. For example in one study 30% of gathering sites have been found to contribute 80% of the total emissions [9]. Identifying and repairing these high emitting sites through LDAR programs is of high importance [10]. Effective LDAR therefore requires finding this small set of large emitters where and when they occur. This naturally necessitates the use of continuous monitoring systems across the entire industry, rather than periodic inspections every few months.

Significant effort has been applied to the development of a range of technologies and systems for monitoring CH_4 emissions on a continuous basis [11]. However, meeting the requirements for deployment at scale in an industry driven by cost reduction and practicality is a significant challenge. This challenge is being actively addressed by a large range of research groups and companies

QLM Technology Ltd. are developing a new Lidar based technology for CH_4 monitoring. The technology is called Tunable Diode Lidar (TDLidar) and is enabled by advances in IR single photon detectors combined with novel signal processing algorithms. The technology has been specifically optimised to provide continuous and widespread monitoring of CH_4 emissions in the oil and gas industry. The purpose of this paper is to describe the technology and investigate its application for use in continuous CH_4 emission monitoring.

We will first briefly explain some of the requirements for the deployment of such technologies in the oil and gas industry and give an overview of other relevant optical gas imaging technologies. We will then give a technical overview of the basic principles behind the operation of the TDLidar gas imager, and present measured performance specifications of the sensor in laboratory conditions. Finally, we will present results of testing the sensor in field trials with controlled CH_4 emissions that were carried out with the National Physical Laboratory (NPL) Emissions and Atmospheric Metrology Group as well as results from a separate measurement campaign at Total SE's TADI (Transverse Anomaly Detection Infrastructure) platform carried out in October 2020.

2. Review and comparison of existing technologies

The majority of total reported methane emissions in the oil and gas industry are due to what are called super emitters, large leaks that, due to their intermittent nature and may not be detected for months at a time. The industry has recognized this is a significant problem, so is looking for more practical ways to effectively implement continuous autonomous monitoring. The U.S. ARPA-E-MONITOR program stated the goal to "*detect and measure methane leaks as small as 1 ton per year from a site 10 m × 10 m in area with a certainty that would allow 90% reduction in methane loss for an annual site cost of $3,000*" [12]. The emission rate target of 1 ton per year equates to about 0.03 g/s or 6scfh. The requirement to reduce emissions by 90% implies some form of continuous (or at least very regular) monitoring will be required industry wide, since the distribution of leaks is characterized by a small number of large leaks [3]. The annual cost requirement of $3,000 precludes many technologies. Particularly it would very likely preclude any technology requiring a human operator for regular site surveys due to the cost of the labour, so the need for continuous and automated monitoring is evident. Cost requirements of $3,000 per year would further seem to preclude technologies with industrial equipment amortisation periods less than ten years that cost more than $20,000. These criteria are a significant barrier to existing offerings.

Overall, it has been observed that there is a clear lack of available technology to locate leaks autonomously with the accuracy needed for a repair crew to find the leak, and beyond that there is an even greater technological and systems challenge to quantify the leak rate and determine the priority for repair. For comprehensive overviews of the different CH_4 detection and quantification technologies and systems see [11,13]. Extensive testing of the performance of the various methane optical detection and quantification has been carried out [14,15]. Here, the advantages and disadvantages of relevant technologies will be briefly discussed, with a focus on comparing the TDLidar gas imaging technology considered here with other optical gas imaging technologies.

2.1. Optical gas imaging (OGI)

The current standard optical imaging technology to locate leaks is to use a handheld optical gas imaging (OGI) camera operating in the mid-wave (3–5 μm) to long-wave infrared (7–14 μm) [16]. These IR cameras can infer the presence of gas by detecting changes in light intensity due to absorption of the gas at infrared wavelengths. They can utilise spectral filters in and out of the imaging path to provide indication of the relative gas concentration [17].

In ideal conditions the technique is effective, but a number of difficulties prevent OGIs use for widespread continuous monitoring. The mid-infrared sensors will typically employ an expensive cooler to keep the sensor at the required temperature for low noise operation. Furthermore, a human operator can be required to operate the camera as OGI cameras have a relatively limited range (tens of meters) for small leaks and poor selectivity between species [16]. Finally unlike the TDLidar technique (and other active illumination methods) OGI is dependent on the thermal background contrast of the gas with the environment, which can affect the signal to noise ratio and require careful interpretation from skilled operators [13]. Although algorithms are being developed for this task [18], quantification remains unreliable.

2.2. Hyperspectral gas cloud imaging (GCI)

A more sophisticated use of infrared sensor arrays is hyperspectral imaging, where light from the environment is spatially separated by wavelength before detection on the sensor array. For the detection of gases hyperspectral imaging is known as hyperspectral Gas Cloud Imaging (GCI) [19]. GCI measures multiple wavelengths of infra-red light per pixel to visualise leaks of target gas species from equipment [20,21].

By sampling a wider range and density of spectra, the technique can be more selective between species, while keeping the high frame rate live video advantages of OGI. However, since the technique is based on passive environmental illumination there is still interference from the thermal background of the scene. Furthermore, the technology is based on long-wave infrared sensor arrays which are less developed for robust long-term deployment compared to standard telecommunications components in the near-IR. Finally, there is a difficult trade-off between either using expensive cooling systems to cool the long-wave IR sensor, or tolerating higher noise operation.

2.3. Tunable Diode laser absorption spectroscopy (TDLAS)

In contrast to techniques like OGI and GCI that rely on passive illumination from the environment for gas sensing, active techniques, illuminate the environment with narrow linewidth laser light. This has the advantage of precisely targeting specific gas absorption line wavelengths to avoid interference from other gas species, and so allows measurement of gas concentration with high accuracy. In addition, the use of active illumination eliminates interference due to background optical (or thermal) effects since the active signal can be modulated in time and space to be clearly distinguishable from any background light.

Laser absorption spectroscopy has been a laboratory technique for many years and is now used industrially with an open laser beam path, and the atmosphere taking the place of the measurement cell [22,23]. Most greenhouse gases have narrow wavelength absorption lines in the short-wave infrared spectral region (around 1.550 μm in wavelength) employed in the fibre optic telecommunications industry. CH_4, for example, has good absorption at 1.6509 μm , and CO_2 has many absorption lines in the telecom region, with 1.572 μm being particularly strong. These lines are widely used in Tunable Diode Laser Absorption Spectroscopy (TDLAS) equipment, employing semiconductor diode lasers that are rapidly modulated to tune in wavelength across a target gas absorption line to measure the exact concentration of a particular gas in the laser path [24,25].

TDLAS systems can be applied for gas imaging in the field by detecting diffusive scattering of the laser off non-cooperative targets in the environment. This approach has the possibility of forming images of gas plumes by scanning the laser beam rapidly around the environment [26]. Systems have also been deployed on unmanned aerial vehicles [27,28]. However, the imaging standoff range is typically limited to 10′s of meters due to the parametric fall in return light intensity with distance. As we will show this range limitation is overcome in TDLidar using a highly sensitive single photon avalanche detector.

2.4. Differential absorption Lidar (DIAL)

Another active illumination technique is Differential absorption Lidar (DIAL) [29]. This involves collecting the backscatter from very powerful laser beams reflecting off aerosol and other particulate matter in the atmosphere, and comparing with laboratory spectra to identify the concentration and spatial distribution of a range of polluting gaseous species over long distances [30,31,32]. This technique offers high-fidelity quantification and localisation, but is large, has a high capital cost, and is non-portable; the DIAL equipment used by NPL, for example, is contained in the trailer of an articulated truck, and requires expert operation and interpretation, presenting a range of logistical challenges to usage in regular surveys [33]. DIAL is a highly effective scientific instrument for large scale total site surveys, but due to its significant cost and size it isn't a viable option for continuous surveillance of individual emissions.

3. TDLidar technology description

We have developed a novel remote gas imaging sensor for application to the detection of gas emissions that builds on some of the key advantages of previously described technologies while avoiding their limitations. The new sensor uses a technique we call Tunable Diode Lidar (TDLidar) and combines aspects of Tunable Diode Laser Absorption Spectroscopy (TDLAS) with Differential Absorption Lidar (DIAL) and Time Correlated Single Photon Counting (TCSPC) to enable remote spectroscopy and ranging with low power semiconductor diode lasers. Our first TDLidar CH_4 sensors use diode lasers with wavelengths around the CH_4 absorption line at 1.6509 μm and Peltier-cooled Single Photon Avalanche Diode (SPAD) detectors in a Random Modulation Continuous Wave (RM-CW) Lidar system. We choose to tune our system to address the CH4 line at 1.6509 μm since here interferences from other atmospheric gases such as H_2O are minimal, and this line has been successfully used for long range Lidar based CH4 measurements previously [34]. The overall system allows long range accurate imaging of gas similar to that obtained by DIAL, but in a much smaller, easily portable design. A photo and general specifications of the sensor are shown in Fig. 1a.

Like TDLAS, TDLidar directly measures the shape of a gas absorption line by continuously sweeping the output wavelength of a diode laser across the absorption line. However, similar to DIAL systems, TDLidar uses a pulsed laser output to encode the light signal and a digital time-domain correlation algorithm between the transmitted and detected light in order to identify the returned light. By simultaneously tuning the laser wavelength and modulating the amplitude it is possible to simultaneously and accurately determine both the range the laser light has travelled, as with typical Lidar, and the amount of a particular gas that the laser light has passed through, as with typical TDLAS.

A fundamental aspect of TDLidar is the use of the high-speed laser tuning, modulation, and detection possible with semiconductor components. This allows the laser wavelength to be scanned at rates of 1 MHz or faster and allows the rapid acquisition of images of both gas spectra and structural distance data over extended fields of view. These high-quality and non-ambiguous three-dimensional images of both the gas and the physical environment it occupies enable the analysis of gas plumes to determine not just the location of the gas, but also assist the calculation of the leak rate that industrial users need.

3.1. Single Photon Avalanche Diode (SPAD) detectors

A major differentiator of the TDLidar CH_4 sensor we have developed is the use of a Short-Wave Infra-Red (SWIR) indium gallium arsenide Single Photon Avalanche Diode (SPAD) detector. These SWIR SPADs are sensitive to single photons of light in the 1.0–1.7 μm wavelength range, where many greenhouse gases absorb radiation (Fig. 2a), and in particular at the 1.65 μm wavelength where CH_4 has a strong absorption line. In addition, these devices operate with low background noise even at temperatures close to room temperature, which is important for practical use. They also have a high bandwidth which is important for building up images quickly for analysis. The high sensitivity of the detector provides the sensor with a long operational range, we have measured gas at more than 100 m distance, while using low power laser components and relatively small light collection optics.

3.2. Optical layout and components

The optical layout of the key components in the TDLidar transceiver system is shown in Fig. 1b. The laser light source is a commercially available multi-quantum well Distributed Feedback Laser (DFB) with an eye-safe 10mW of output power. The DFB laser is driven by a periodically varying current with around a 1 MHz period that scans the output wavelength across the CH_4 absorption line (Fig. 2b). We apply the required binary amplitude modulation required for the lidar scheme to the DFB laser output by passing it through a commercially available optical modulator. A key principle of the optical design is the use of a single co-axial optical transmit and receive axis, coupled via a polarising beam splitter (labelled PBS in Fig. 1b). This maintains the transmit and

Technology	Tunable Diode Lidar Gas Sensor
Laser Wavelengths	Eyesafe IR (1651nm)
Laser Output Power	10 mW (Class 1M)
Sensor Size	125 x 140 x 400 mm (W x H x L)
Weight	6.1kg (or 8.1kg with pan/tilt stage)
Pan Tilt range	350° horizontal and 0-60° vertical
Environmental Robustness	IP64. Operating temperature 0-40°C
Power Consumption	21 W (including pan tilt stage)

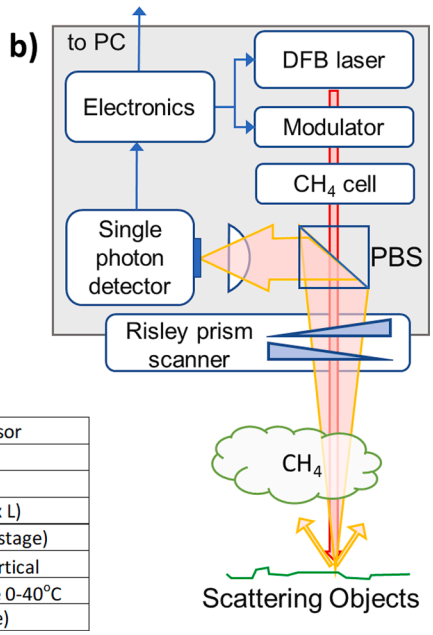

Fig. 1. Tunable Diode Lidar (TDLidar). (a) Photo of prototype system and system specifications. (b) Schematic of the internal layout of the system. Transmitted light is generated via DFB laser, then passes through the optical modulator and a 1000 ppm.m CH_4 cell. The light is scanned around the environment by a standard Risley prism pair scanner. Scattered light returns to the same aperture. A polarizing beam splitter (PBS) directs 50% of the received light into a single photon detector.

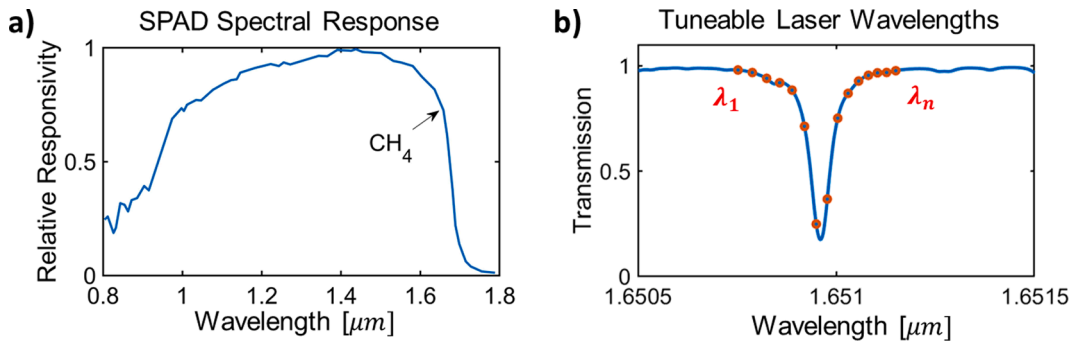

Fig. 2. a) Spectral response of the sensors SWIR SPAD (Short-Wave InfraRed indium gallium arsenide Single Photon Avalanche Detector) indicating the location of the CH4 absorption line at 1.6509 μm . b) Illustrative diagram showing the CH4 absorption line and the and the set of wavelengths measured by the TDLidar sensor (red dots).

receive path alignment over long ranges, while the polarisation purity of the output and the polarisation selection of the beam splitter protects the highly sensitive SPAD from direct laser light reflections inside the device. Finally, we use a mechanically rotated Risley prism pair [35] to rapidly scan the transmitted beam across the scene and build up an image. For the results presented in this work one prism of the pair was rotated at around 0.5 Hz while the other was rotated at around 1.5 Hz. After diffusive scattering off objects in the environment a tiny fraction of the scattered light ($\sim 1/10^8$) returns to the transceiver. At the polarising beam splitter 50 % of the returning light is directed towards the SPAD where it is detected. Typical return light levels are in the range of tens to hundreds of picowatts.

3.3. Photonics and signal processing

The photonic system of the TDLidar sensor is depicted schematically in Fig. 3. Both continuous wavelength tuning and pseudo-random amplitude modulation are applied to the laser light [36]. Previously similar amplitude modulation approaches have been applied in conjunction with a single photon detector and two independent laser wavelengths previously for the detection of CO_2 [37]. Instead of just sampling the gas absorption feature at two laser wavelengths, the TDLidar system presented here works by continuously tuning the DFB laser across the gas absorption line at a rate of approximately 1 MHz (i.e. 1 μs period), and then the light is independently amplitude modulated (using the optical modulator) on and off with a pulse duration of around 10 ns per bit. The amplitude modulation and subsequent convolution of the return signal with the output allows the system to independently measure both the wavelength and the time of flight of the return signal. We can therefore produce a spectrum of the CH_4 1.6509 μm absorption line with multiple wavelengths as shown by the dots in Fig. 2b. For high-speed imaging a signal integration time of 10 ms, is used to accumulate enough data to accurately measure the absorption curve and gas concentration. This gives the sensor a base data acquisition rate of 100 CH_4 measurements per second (i.e. 100 Hz). We will expand on this point in Fig. 5 later in the paper.

The DFB laser is modulated in wavelength back and forth across a CH_4 absorption line at 1.6509 μm using a square wave laser drive current with period 1 μs as shown in Fig. 3a. Both the high and the low current states are above the lasing threshold for the laser, and the equilibrium temperature and output wavelengths differ for the high and low input currents. Thus, the temperature of the laser gain medium oscillates

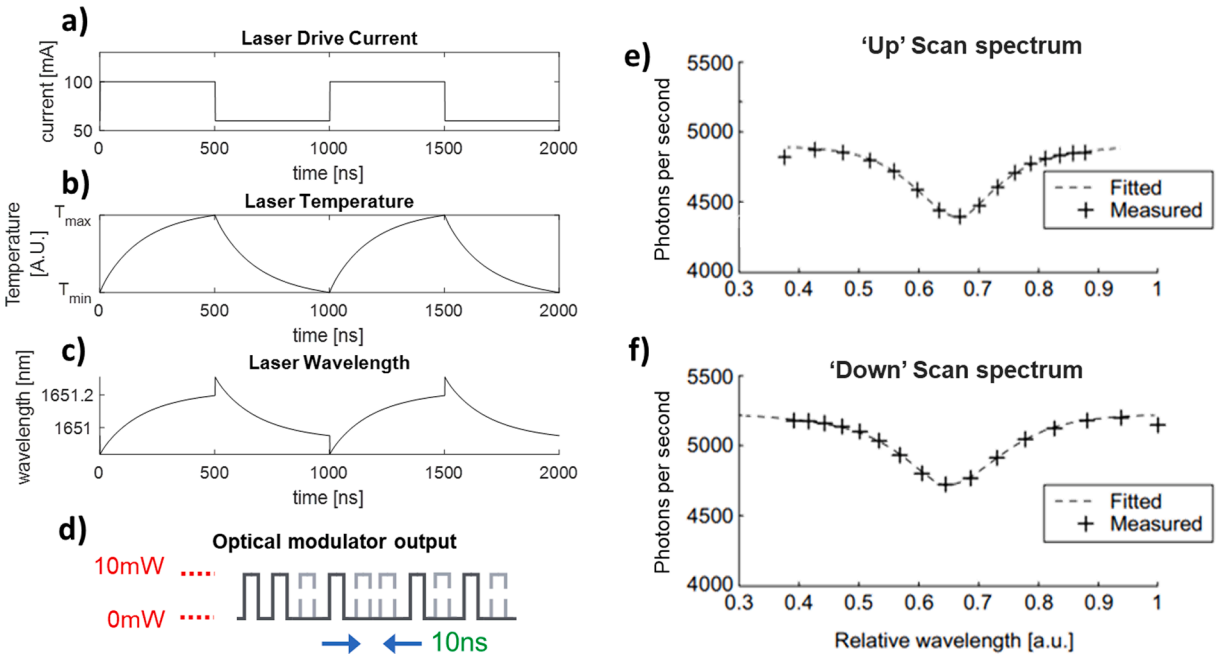

Fig. 3. Photonic system. a) Laser current modulation at 1 MHz. b) Temperature change of laser induced by current modulation. Note that only the qualitative shape of the temperature curve is known so T_{min} and T_{max} were used to represent the unknown temperature limits. c) Laser output wavelength induced by combined current changes and temperature changes. d) diagram of rapid amplitude modulation of laser to create CW-RM (continuous wave random modulation) lidar system. e)-f) Simulation of CH_4 absorption spectrum for the 'up' and 'down' wavelength scans. Note that a)-e) are all numerically generated illustrations, not experimental data.

between the two steady state temperatures with 1μ s period, and similarly the laser wavelength is continuously tuned between two different wavelengths limits as shown in Fig. 3b-c. The laser output wavelength is affected instantaneously by both the number of free carriers in the gain medium and the temperature of the gain medium. This explains why the DFB wavelength jumps when the injection current is changed, and thereafter smoothly tunes due to the slower temperature changes between the two equilibrium states [38]. This smooth continuous tuning across the CH_4 line is used for spectroscopy in the TDLidar system. After the continuous wave laser light is generated by the DFB laser it is passed to the optical modulator (labelled modulator in Fig. 1b). The modulator applies an amplitude modulated pseudo random binary pattern to the laser light as shown in Fig. 3d. This pattern allows the return signal to be distinguished from background light and random noise when detected by the SPAD sensor.

A simulation of the spectrum that would be measured using this scheme is shown in Fig. 3e-f. Here the '+' points represent wavelengths that are measured by the sensor while the dashed line is a curve fitted to those data points applying the Beer-Lambert law and assuming a Lorentzian absorption cross section. The density of measured spectral points

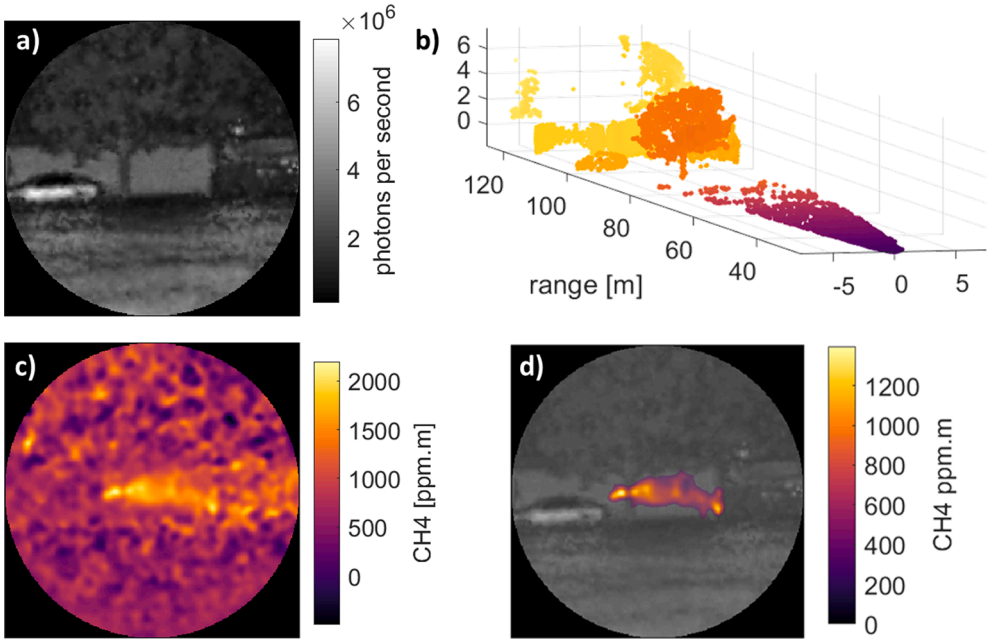

Fig. 4. TDLidar imaging data examples. a) sensor signal level image. b) Lidar point cloud (colour indicates distance from sensor). c) CH_4 concentration path length (ppm.m) image and d) CH_4 concentration path length plume extracted from c) with a background level change, and overlaid on the signal level image a).

is higher on the right-hand side of Fig. 3e since the laser is scanning up in wavelength, and the scanning rate slows as the laser gain medium approaches thermal equilibrium (and vice-versa for the down scan in Fig. 3f).

3.4. TDLidar data visualisation

TDLidar uses the relative depth of the measured absorption curve to determine the gas concentration path length product, typically expressed in parts per million times meters (ppm.m). The sensor accumulates data points at a rate of 100 Hz while the beam is rapidly scanned around the environment. After accumulating several thousands of points the data can be visualized in two- and three-dimensional images. The data is complex, containing signal intensity, Lidar range and spectral information. Because of this there are a number of different ways to visualise it.

Fig. 4 describes the typical formats for visualising TDLidar data. Firstly, like a normal visual camera, the basic intensity level of the returned signal can be imaged spatially, as shown in Fig. 4a. Here we can see a tree, a car and a wall at a range of around 100 m. White areas are high signal and dark areas are low signal. Acceptable signal levels for accurate CH_4 measurement can be as low as 0.7×10^6 photons per second. Next, a typical Lidar distance point cloud is generated. The same data set is plotted in Fig. 4b showing the ranges of the various objects in the scene both in a three-dimensional plot and by colour. The CH_4 concentration path length image for the same data set is shown in Fig. 4c. There is a background CH_4 level of around 600 ppm.m, due to the ambient CH_4 in the atmosphere and a 500 ppm.m contribution from the internal CH_4 cell in the sensor. Note that since the laser passes twice through the gas in the environment the measured ppm.m is divided by two to give accurate results. This causes the internal 1000 ppm.m cell to read as 500 ppm.m since the laser only passes once through the cell. The noise level in the CH_4 image is fairly high (106 ppm.m using 1 s averaging time) due to the long range from which the signal is returning (100–120 m). Finally, in Fig. 4d the CH_4 plume is isolated by subtraction of the background due to the internal gas cell and ambient gas in the atmosphere, followed by applying a plume detection algorithm that simply identifies and separates out large connected regions of elevated CH_4. The plume image is overlaid on the original signal level image from Fig. 4a. This is the standard image used to identify both the location and size of the plume for the remainder of this publication. It is of interest to note that all images appearing in the form of similar to Fig. 4d are generated automatically by the plume detection algorithm rather than by manually identifying the plume.

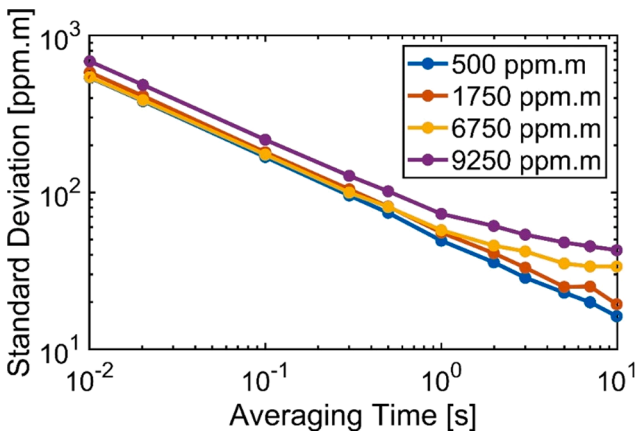

Fig. 5. Measurement standard deviation for varied measurement averaging time (x-axis) and different amounts of CH_4 (line colour). The inverse square root slope indicates random noise being reduced by increased averaging time.

3.5. Leak rate estimation

Estimation of leak flow rate is of considerable interest to the overall quantification method: Understanding the leak rate of individual sources informs prioritisation of a repair schedule, facilitating the greatest reductions in emission in the short term. Once a CH_4 plume is identified the TDLidar sensor currently uses a simple mass balance approach to calculate the gas flow rate [39], although there is significant scope for more sophisticated algorithms to be applied. The mass balance approach aims to determine the flow rate by calculating the mass of gas flowing through a three-dimensional surface enclosing a gas source. The mass flux is defined as the mass of gas passing through a surface per unit area per unit time. By integrating the mass flux through a set of planes enclosing a volume the total flux of gas entering or leaving that volume can be found. If the net flux is non-zero this indicated that the region is emitting gas. The mass flux through a plane is defined as

$$\Phi = \rho \boldsymbol{v} \bullet \boldsymbol{A}$$

where ρ is the gas concentration (g/m^3), $\boldsymbol{v}$ is the wind velocity vector, and $\boldsymbol{A}$ is the area vector of the plane. For the case of TDLidar the beam measures a concentration path length rather than the point density of CH_4. The equation is adapted to set one dimension of the plane $\boldsymbol{A}$ to be the laser beam vector times the concentration path length ($\boldsymbol{\xi}$), and the other edge to be a vector length $\boldsymbol{l}$ perpendicular to the laser beam. Then $\boldsymbol{A}\rho = \boldsymbol{l} \times \boldsymbol{\xi}$ where the vector $\boldsymbol{l}$ is the side of the plane perpendicular to the laser and $\boldsymbol{\xi}$ is the vector of the laser beam concentration path length (units of g/m^2). This vectorisation allows the mass balance algorithm to be applied to the images data produced by the TDLidar sensor in a similar manner similarly to many previous works [39,28].

4. Results

4.1. Sensor metrological validation

Validation of the sensor under laboratory conditions was undertaken using calibrated CH_4 gas cells to create a range of different concentration path lengths. The measurements evaluated both the precision and accuracy of the CH_4 measurements produced by the sensor. The precision was analysed with respect to varied measurement averaging time and concentration path length values. The accuracy measurements used a long measurement time (10 s) to reach a high level of precision, then checked the discrepancy between the sensor reading and the true CH_4 concentration path length.

The Allen Deviation is a metric that is commonly applied to evaluate the precision of sensors over varied averaging times [40]. We tested the Allen Deviation of the sensor by disabling the scanner system and directing the beam at a fixed diffusive target 5 m from the sensor. The laser beam was attenuated significantly to ensure a return signal of 2 mega-counts of photons detected per second (Mcps). This signal level corresponds to typical long range signal return levels for the sensor operating up to 200 m (depending on surface scattering coefficient). Different concentration path lengths of CH_4 were achieved by placing various combinations of calibrated CH_4 gas cells in the external beam path of the sensor. The gas cells contained varied mixtures of CH_4 and nitrogen at atmospheric pressure. The cells had CH_4 ppm.m values of 500, 1250, 2500 and 5000 ppm.m, and by combining multiple cells in series the sensor precision could be tested for concentration path lengths ranging from 500 ppm.m to 9250 ppm.m.

The results of the precision testing are shown in Fig. 5. The y-axis shows the standard deviation of the sensor CH_4 concentration path length measurements, while the x-axis shows the amount of averaging used on raw the 0.01 s data points to obtain the measurements. For example, an averaging time of 1 s means that 100 of the raw 0.01 s CH_4 readings were averaged together to produce one higher precision CH_4 measurement. The standard deviation of a large set of these 1 s averaged measurement is then calculated to find the sensor precision for 1 s

averaging time.

As expected, precision improved with averaging time (τ). The precision follows the maximal $1/\sqrt{\tau}$ scaling until around 1 s averaging time. For longer averaging times low frequency noise sources begin to affect the precision. We believe this low frequency noise is due to fluctuations in the laser wavelength tuning. This effect is more pronounced for the higher ppm.m measurements due to the inverse exponential relationship between gas concentration path length and transmission amplitude (described by the Beer-Lambert law). In other words, the same sized fluctuation in laser amplitude causes a larger absolute change in ppm.m if the ppm.m level is higher. The maximum averaging time presented here is rather short (10 s), and in future, lab tests will be carried out evaluate the drift on multi-hour time scales. Anecdotally, the field trial presented later in this manuscript suggests stability of the sensors background ambient ppm.m readings to within ±200 ppm.m over multiple days.

Further testing was carried out to test the accuracy of the sensor to known CH_4 concentration path lengths. The accuracy was tested in two configurations. Firstly, the sensor accuracy was tested in a lab setting with a scattering target at 5 m range and a selection of different combinations of calibrated CH_4 gas cells (Fig. 6). In this case the sensor laser beam was attenuated to two different levels (1 Mcps and 3 Mcps) per concentration path length value to emulate high signal return levels and low signal levels. The measured and actual values of the cells for signal levels of 1 Mcps and 3 Mcps are shown in Fig. 6a and Fig. 6b respectively. The measurement averaging time used for these measurements was 10 s. The resulting CH_4 readings very closely match the true cell ppm.m values, as shown by the close agreement of the data points to the expected ppm.m line in Fig. 6a-b. This verifies that the CH_4 ppm.m reading is not influenced significantly by the signal level.

The error between the measured and actual ppm.m values of the cells is shown in Fig. 6c and Fig. 6d for the 1 Mcps and 3 Mcps signal levels respectively. The error is defined as the difference between the true and measured concentration path lengths. The results show there is a certain amount of systematic error, although it is typically less than 100 ppm.m. The average of the measurement error at for the 1 Mcps data is 33 ppm.m and the average error for the 3 Mcps data is 54 ppm.m. This level of accuracy is around 10% of the CH_4 concentration path length values produced by small leaks of 0.012 g/s (see Fig. 8c later). These systematic errors are likely caused by non-uniformity of the laser spectrum. A slight bend in the output spectrum caused by internal photonic effects can increase or decrease the apparent depth of the CH_4 absorption line shape. However, as shown the resulting error from this effect is minimal for concentration path length accuracy required for emissions detection. It is also worth noting there is a small amount of uncertainty about the exact beam path length through the cell, which will also contribute to the systematic error.

Further testing was carried out with the scanner now operating to scan the beam around the environment outdoors. This allows the sensor to acquire data from a variety of different ranges to generate a more representative data set. A plot of the observed CH_4 concentration vs range is shown in Fig. 7. When the scanner is in motion the beam does not dwell on one spot, so the measurement averaging time of 10 s is

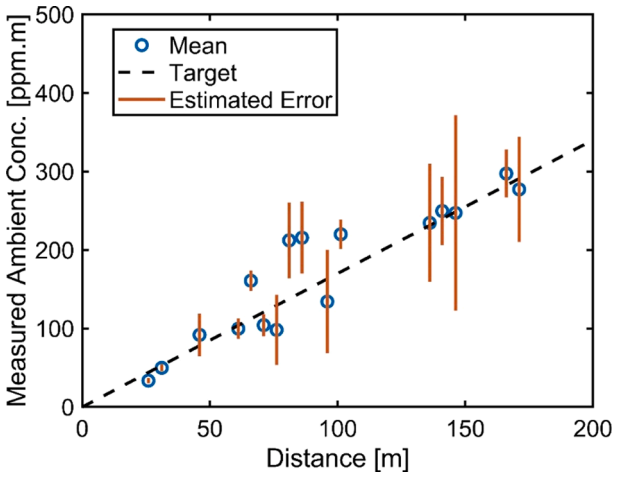

Fig. 7. Measurement of the ambient CH4 in the atmosphere at varied ranges. The expected ~ 1.8 ppm ambient level is shown as a dashed line. The precision varies with range due to the signal reflection level off different objects.

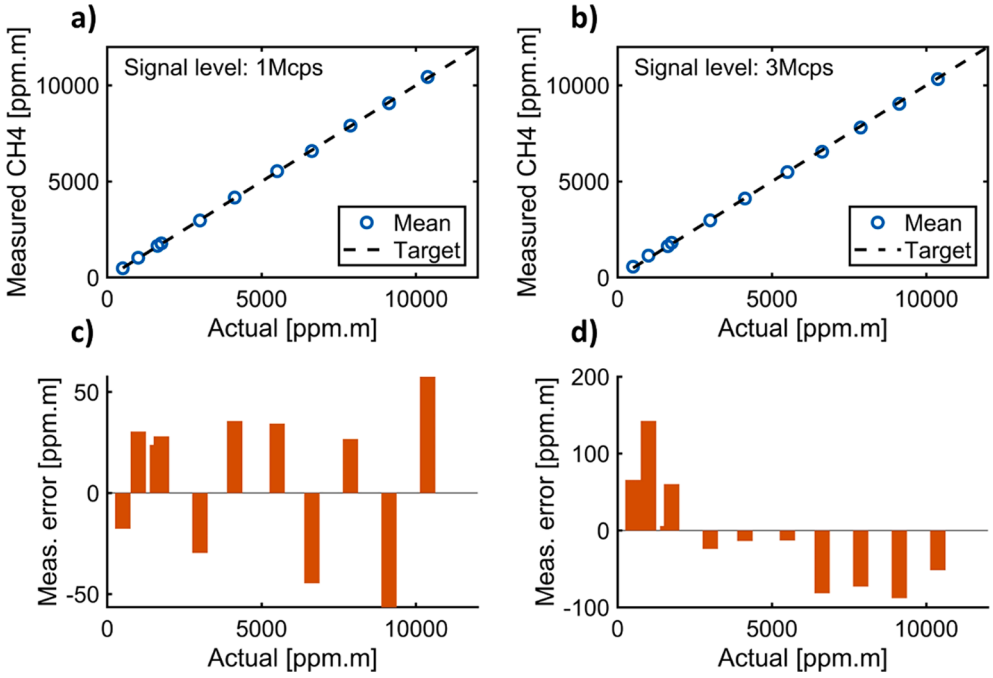

Fig. 6. CH_4 measurement accuracy. a)-b) Measurement of CH_4 concentration pathlength (ppm.m) with calibrated gas cells. Sensor readings compare accurately with the known calibrated gas cell values. c) and d) show the corresponding error between the measured ppm.m values and the actual calibrated cell ppm.m values.

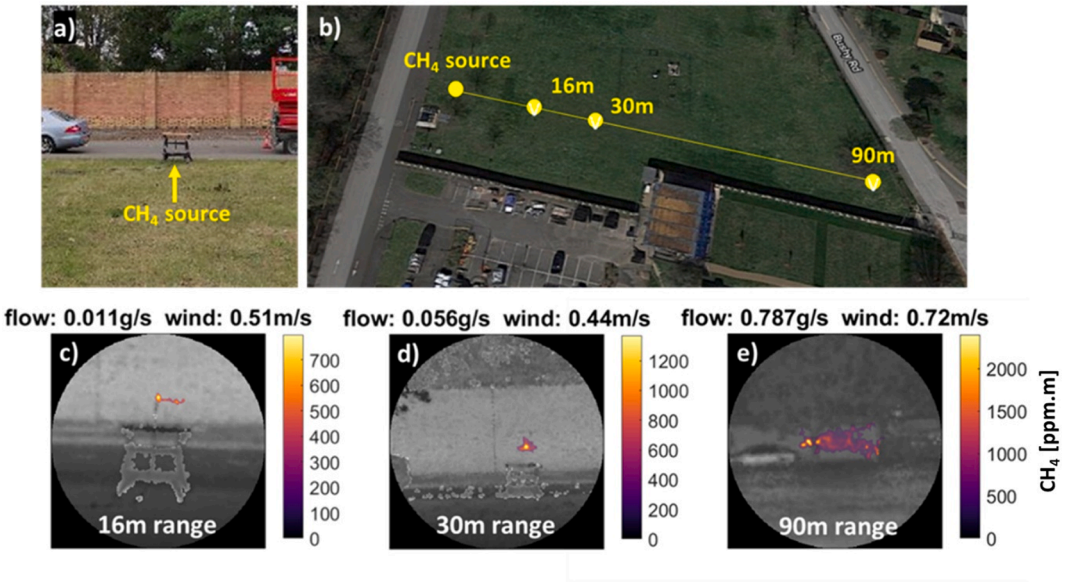

Fig. 8. Calibrated CH_4 leak imaging. CH_4 plumes of varying sizes were created with a calibrated piped CH_4 supply and measured at varying distances and environmental wind conditions. The experimental setup is shown in a) and b). Images c)-e) show examples of ppm.m plume images overlaid on the signal level image as described in Fig. 4d. Trials were conducted at the National Physical Laboratory in Teddington UK.

achieved by picking non temporally sequential data points from nearby spatial areas. This has the effect of increasing the time range over which the data points are averaged, thus increasing exposure to low frequency noise. Therefore, the precision is lower when the beam is scanning than in the case of a stationary measurement as in Fig. 5. Regardless, the result achieved in Fig. 7 closely matches the expected ambient 1.8 ppm concentration of CH_4. The best linear fit to the measured data has a slope of 1.67 ppm, an offset of + 13.4 ppm.m, and an R^2 value of 0.84.

4.2. Field trials with the National Physical Laboratory

A campaign of field trials was undertaken at the National Physical Laboratory. The prototype TDLidar camera was used to image controlled releases of CH_4 in an outdoor setting. Measurements were made at a range of distances and release rates, in varying environmental conditions (both natural and artificial). A flow control system similar to reference [30] was used to control the release rate of CH_4.

Fig. 8 illustrates the experimental setup for varied sensor range and flow rate measurements. The camera was placed at several distances from a mounted release tube connected to a mass flow controller. CH_4 was nominally released at between 0.012 g/s and 0.835 g/s (the mass flow controller used units of litres per minute, and these values corresponded to 1 L/min to 70 L/min). Measurements were taken from distances between 16 m and 90 m from the CH_4 release point with the sensor directed horizontally across a field and a backdrop of trees and a brick wall for laser scattering as shown in Fig. 8a and b. The backdrop was around 15 m behind the CH_4 release point.

Typical results from measurements in this configuration are shown in Fig. 8c-e . Each image corresponds to a measurement time of approximately one hundred seconds (i.e. 10,000 of the 10 ms duration CH_4 readings). Releases of as low as 0.012 g/s were imaged from the shorter 16 m range. However, at longer ranges the 0.012 g/s release was not detected. Releases of 0.056 g/s were imaged clearly from up to 30 m range, while the 0.835 g/s was easily detectable from 90 m. Based on the relative size and high ppm.m values detected in the 0.835 g/s release we estimate that this would be detectable at up to 200 m range, though due to the limited size of the field this was not verified experimentally.

We note that the absolute ppm.m values of the small leak of 0.011 g/s in Fig. 8c are above 700 ppm.m. Looking at the longer range measurements in Fig. 8d-e it is clear that ppm.m levels of 700 ppm.m are resolvable at much longer ranges than 16 m. Thus, the failure of detection of the small leak at longer ranges than 16 m is not due to the CH_4 concentration path length of the small plume being too low for detection. Thus, the reason that the small leaks were not detected at longer range is likely because the much smaller solid angle occupied by the plume reduced the probability the laser would intersect the plume.

In summary larger CH_4 releases were easily detectable at the longer ranges, while shorter range measurements were able to detect and visualise even the smallest releases. The limitation in detection of small releases at long range was caused by the spatial resolution and precise control of the scanner laser system, rather than a lack of sensitivity to low ppm.m levels, or range of the optical transceiver system. Since the laser beam diameter is around 20 mm, it is expected that small gas release (0.01 g/s) could be resolved at long ranges (hundreds of meters) if the laser directly intersected the plume.

An important factor in imaging and quantifying gas emissions is the speed of the wind. Variable wind speeds were created using an artificial source in the form of a large fan, illustrated in Fig. 9a. An anemometer was positioned in the path of the fan, close to the CH_4 source, to monitor the local air flow speed. This setup allowed simulated wind to be applied to the CH_4 source with speeds of 1 m/s to around 10 m/s.

On this occasion, the sensor was deployed at height using a mobile elevated work platform (MEWP), looking down over a short distance perpendicular to the flow of wind generated by the fan as shown in Fig. 9b. The background of the image was the grassy field around 13 m from the sensor. Release rates and artificial wind speeds were varied to evaluate the limit at which wind speed reduced the effectiveness of the measurement.

The variation in wind produced an expected variation in the shape of the plume, demonstrating the capability of the TDLidar sensor to resolve spatial variations in plume structure. High wind velocity caused narrow and straight plumes, while lower wind velocity produced border plumes with a gentle curve towards the wind direction (Fig. 9c-h). At higher wind velocities, some smaller releases are sufficiently diluted by the air flow to make them more difficult for the camera to detect, resulting in less obvious visualisation and higher uncertainty in the flow rate calculation. It should be noted, however, that the artificially induced wind was constant, which is unlikely to be true of conditions experienced in real-world environments. It seems likely that capability to image the way the plume changes shape and density over time could

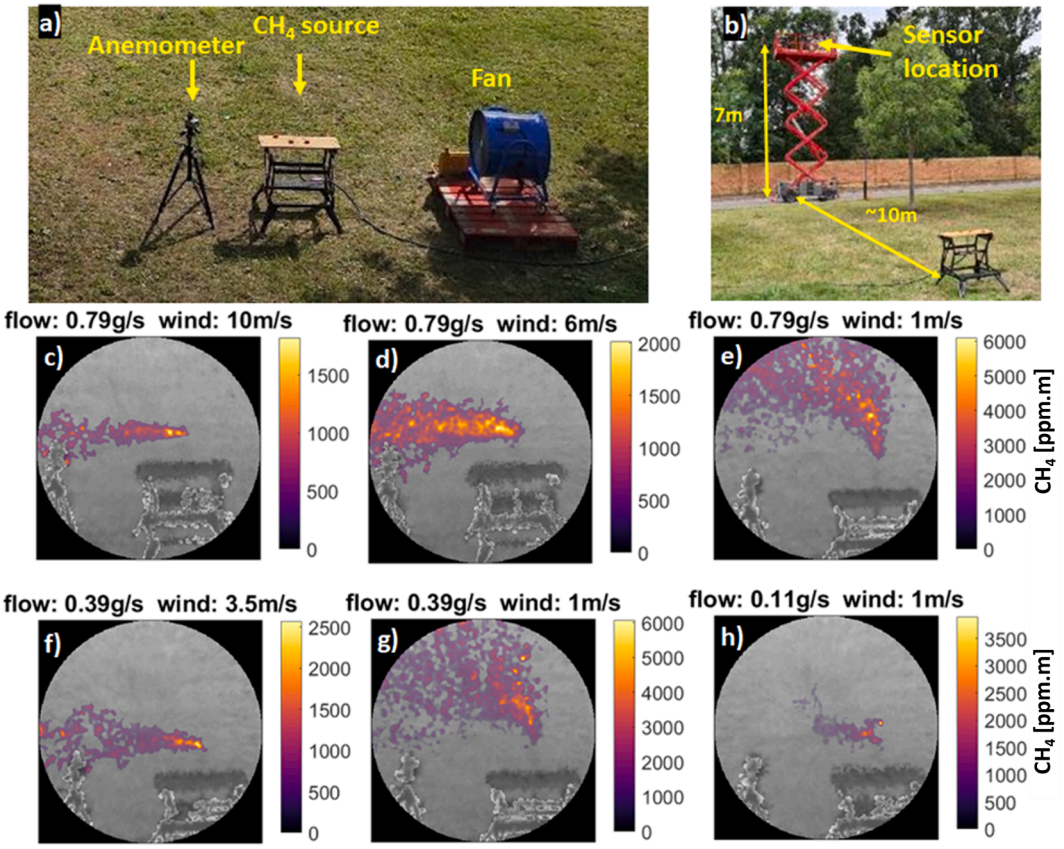

Fig. 9. CH_4 leak imaging with controlled wind conditions. CH_4 plumes of varying sizes were measured at varying wind speeds. The experimental setup using a large fan to vary winds speed at the plume is shown in a) and b). Images c)-h) show example results for various combinations of wind speed and CH_4 flow rate.

provide information about the local wind speed [41] which would be useful for flow rate estimation.

Flow rates were estimated using the simple mass balance algorithm applied to the entire data set acquired during the trial. An anemometer positioned at roughly 1 m height was used to record the wind speed with one-minute time resolution which was then used in the mass balance calculation. The flow rate estimation results for all tests at NPL using the TDLidar sensor are shown in Fig. 10. This includes results from measurements with high (artificial) wind and long range. The correlation between calculated leak flow rate and actual leak flow rate is strong considering the simple flow algorithm and variety of wind speeds and ranges. Across the whole set there is an average percentage error of around 50 % between the estimate and the true flow value. We believe this can be significantly improved as we continue to refine the sensor performance and our flow rate calculations, but the current results indicate very good potential for accuracy at the level needed for effective industrial monitoring.

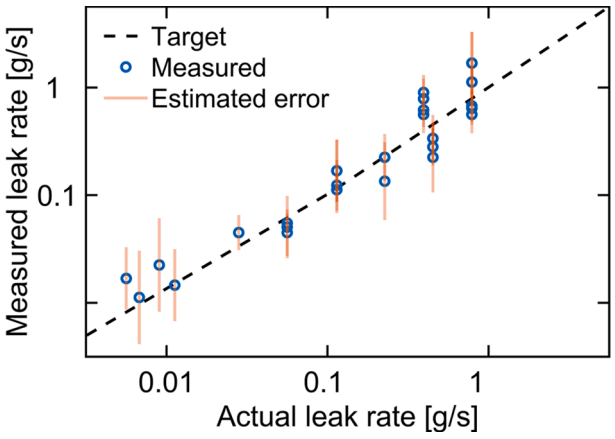

Fig. 10. CH_4 leak flow rate measurement accuracy. Comparison of calculated leak flow rate and calibrated leak rate for all measurements during the NPL field trial.

5. Preliminary industrial trials with total

QLM was invited to take part in blind CH_4 emission monitoring tests run by Total SE on their TADI (Transverse Anomaly Detection Infrastructure) platform in Lacq, France. These trials involve leak detection and quantification equipment being set up around a dedicated zone that contains various typical industrial infrastructure such as tanks and pipes. The site has been extensively plumbed with an array of gas supply pipes and valves so that deliberate quantified leaks from 0.01 g/s to greater than 100 g/s of CH_4 can be released on demand. The challenge for the equipment is to demonstrate the ability to detect, localise and quantify blind releases (unknown location and unknown release rate). One “non-blind” release with known flow rate was made, for calibration purposes, after which the leak detection equipment under test needed to identify the location, and calculate the release rate, of leaks generated over the site.

Fig. 11 shows some examples of data taken in these TADI tests. Fig. 11a) is an image of a CH_4 plume overlaid on a full-colour image taken with an onboard visual camera. This represents an approximation of a CH_4 emission in a real industrial facility and demonstrates the potential of the technology to localize emissions in complex industrial settings. Fig. 11b and c show the TDLidar sensor’s view of large and small leaks situated about a storage tank as examples in the style of the previous images in the paper.

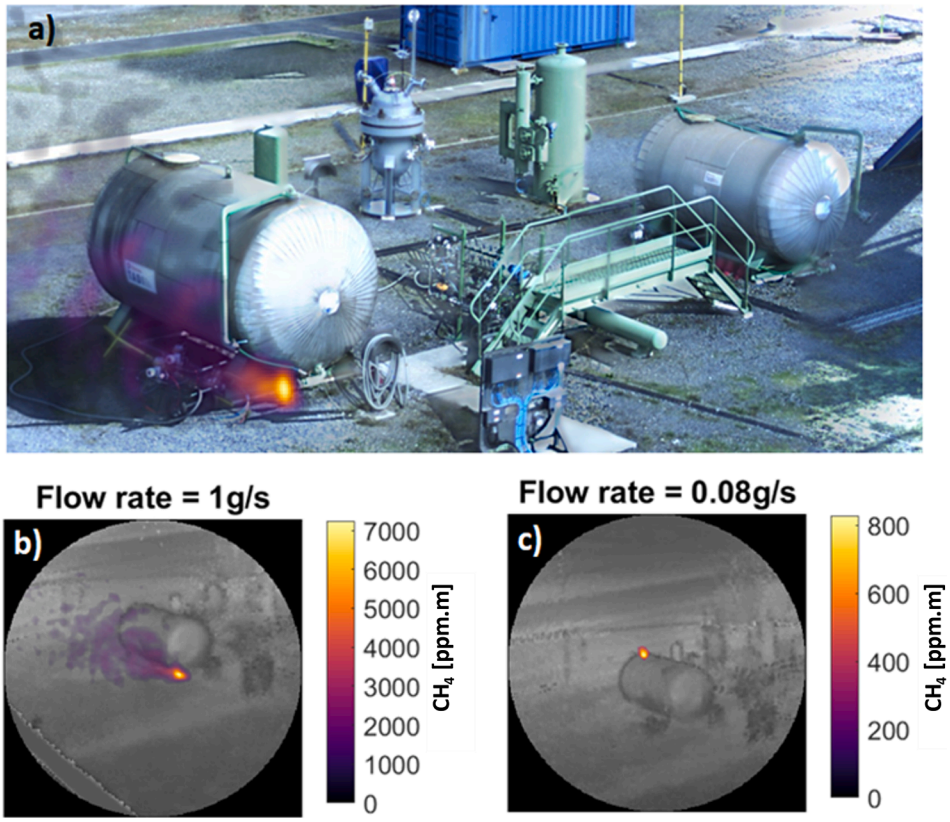

Fig. 11. CH_4 release measurement in an industrial environment. TDLidar images of CH_4 releases test at Total's TADI (Transverse Anomaly Detection Infrastructure) platform at Lacq, France. a) CH_4 plume image overlaid on full-colour background image from visual camera b) and c) CH_4 ppm.m plume images overlaid on the infrared signal level image as described in Fig. 4d. Data acquired at the Total TADI 2020 CH_4 Quantification Blind Test trials.

During the duration of the field testing the metrological strengths of the TDLidar system over existing solutions were established its long-range imaging ability combined with quantitative ppm.m readings that are unaffected by environmental factors such as ambient lighting or temperature contrasts. Weaknesses of the system include its data acquisition speed (100 s per image) and need for a solid scattering target to return the laser light to the sensor. However, we note that these perceived weaknesses are shared by most active sensing-based technologies. Furthermore, for the case of continuous autonomous monitoring the measurement duration would not be a significant issue, and the availability of suitable backscattering targets could be ensured by placing the sensor at a high vantage point (as shown in Fig. 11).

6. Conclusions

To reduce CH_4 emissions and slow global warming there is a widespread and growing need for effective and scalable CH_4 monitoring techniques that are deployable at industrial scale. Continuous monitoring of CH_4, as opposed to intermittent monitoring via surveys, offers the opportunity to enable and verify CH_4 emissions reduction programs by providing greater certainty in CH_4 budgets, eliminating estimation, and indicating where the greatest reductions can be made in the shortest possible time frame. Government regulations are rapidly changing to reflect this, and the oil and gas industry has committed to adopt a more effective CH_4 monitoring and reporting strategy.

Continuous monitoring of emissions in the oil and gas industry is a major challenge due to the stringent cost requirements of the industry and the obvious need for high durability, long lifetime, and complete autonomy. In this paper we have demonstrated a unique Tunable Diode Lidar gas imaging technology that meets these requirements. It utilises mature, robust, and highly cost effective and scalable near-infrared telecommunications components in a unique configuration for spectroscopic Lidar. The technology provides accurate CH_4 concentration imaging using an active scanning technique that can cover ranges of hundreds of meters. We have presented results of field trials of this technology carried out with the help and support of the National Physical Laboratory. This has demonstrated the capability of the technology for imaging CH_4 emissions nominally as low as 0.012 g/s and larger leaks at ranges of up to 90 m. We have also previewed some results of trials at TOTAL's TADI platform where we demonstrated the sensor operating in a realistic industrial facility. We are continuing to apply this technology to industrial applications with the help of end users, including the UK National Physical Laboratory (NPL), National Grid Gas, BP and AMETEK Land.

The immediate target products are a fixed emplacement camera, mounted on a pan/tilt system to survey a wide area from a single point, on a rugged and durable platform suitable for use in industrial environments. The quantitative accuracy of the sensor, high quality of the multiple images it captures, and lack of background interferences, means we expect our leak detection and quantification to be reliable and autonomous. The next step will be to make the platform faster, smaller and lighter, enabling deployment on mobile platforms such as UAVs. Of particular interest is autonomous UAV monitoring, which removes the cost of the operator, and tethered versions which remove limitations on flight time. We believe these solutions can be at the forefront of regulatory development, and provide operators with the means to both comply, and to reach ambitious Net-Zero carbon targets, on a readily available, cost effective platform.

Declaration of Competing Interest

The authors declare that they have no known competing financial

interests or personal relationships that could have appeared to influence the work reported in this paper.

Acknowledgements

We are grateful for funding support from the University of Bristol, the National Quantum Technology Programme, Innovate UK via the Analysis 4 Innovators Round 4 Phase 2 project no. 105579, the Emissions and Atmospheric Metrology Group at the National Physical Laboratory, and from Total SE France. Particular thanks to John Rarity at University of Bristol and Jon Helmore and Nigel Yarrow at NPL for their generous support in time and discussions.

References

[1] Stocker T, Qin D, Plattner G, Tignor M, Allen S. "Climate Change 2013: The physical science basis. contribution of working group I to the fifth assessment report of IPCC the intergovernmental panel on," 2014, Accessed: Jan. 22, 2021. [Online]. Available: https://boris.unibe.ch/71452/.

[2] Etminan M, Myhre G, Highwood EJ, Shine KP. Radiative forcing of carbon dioxide, methane, and nitrous oxide: A significant revision of the methane radiative forcing. Geophys Res Lett 2016;43(24):12614–23. https://doi.org/10.1002/2016GL071930.

[3] Thompson RL, Stohl A, Zhou LX, Dlugokencky E, Fukuyama Y, Tohjima Y, et al. Methane emissions in East Asia for 2000–2011 estimated using an atmospheric Bayesian inversion. J Geophys Res Atmos 2015;120(9):4352–69. https://doi.org/10.1002/2014JD022394.

[4] Shindell D et al. "Simultaneously mitigating near-term climate change and improving human health and food security." Science (80-.)., vol. 335, no. 6065, pp. 183–189, Jan. 2012, doi: 10.1126/science.1210026.

[5] Maasakkers JD, Jacob DJ, Sulprizio MP, Scarpelli TR, Nesser H, Sheng J-X, et al. Global distribution of methane emissions, emission trends, and OH concentrations and trends inferred from an inversion of GOSAT satellite data for 2010–2015. Atmos Chem Phys 2019;19(11):7859–81. https://doi.org/10.5194/acp-19-7859-2019.

[6] Schwietzke S, Sherwood OA, Bruhwiler LMP, Miller JB, Etiope G, Dlugokencky EJ, et al. Upward revision of global fossil fuel methane emissions based on isotope database. Nature 2016;538(7623):88–91. https://doi.org/10.1038/nature19797.

[7] Saunois M, Bousquet P, Poulter B, Peregon A, Ciais P, Canadell JG, et al. The global methane budget 2000–2012. Earth Syst Sci Data 2016;8(2):697–751. https://doi.org/10.5194/essd-8-697-201610.5194/essd-8-697-2016-supplement.

[8] Y. Zhang *et al.*, "Quantifying methane emissions from the largest oil-producing basin in the United States from space," *Sci. Adv.*, vol. 6, no. 17, Apr. 2020, doi: 10.1126/sciadv.aaz5120.

[9] Mitchell AL, Tkacik DS, Roscioli JR, Herndon SC, Yacovitch TI, Martinez DM, et al. Measurements of methane emissions from natural gas gathering facilities and processing plants: Measurement results. Environ Sci Technol 2015;49(5):3219–27. https://doi.org/10.1021/es5052809.

[10] Zavala-Araiza D, Alvarez RA, Lyon DR, Allen DT, Marchese AJ, Zimmerle DJ, et al. Super-emitters in natural gas infrastructure are caused by abnormal process conditions. Nat Commun 2017;8(1). https://doi.org/10.1038/ncomms14012.

[11] Fox TA, Barchyn TE, Risk D, Ravikumar AP, Hugenholtz CH. A review of close-range and screening technologies for mitigating fugitive methane emissions in upstream oil and gas. Environ Res Lett 2019;14(5):053002. https://doi.org/10.1088/1748-9326/ab0cc3.

[12] "MONITOR | arpa-e.energy.gov." https://www.arpa-e.energy.gov/technologies/programs/monitor (accessed Jan. 31, 2021).

[13] Hagen N. Survey of autonomous gas leak detection and quantification with snapshot infrared spectral imaging. J Opt (United Kingdom) 2020;22(10):103001. https://doi.org/10.1088/2040-8986/abb1cf.

[14] A. P. Ravikumar *et al.*, "Single-blind inter-comparison of methane detection technologies – results from the Stanford/EDF Mobile Monitoring Challenge," *Elem. Sci. Anthr.*, vol. 7, Sep. 2019, doi: 10.1525/elementa.373.

[15] C. S. Bell, T. Vaughn, and D. Zimmerle, "Evaluation of next generation emission measurement technologies under repeatable test protocols," *Elem. Sci. Anthr.*, vol. 8, Jul. 2020, doi: 10.1525/elementa.426.

[16] A. P. Ravikumar, J. Wang, and A. R. Brandt, "Are Optical Gas Imaging Technologies Effective for Methane Leak Detection?," *Environ. Sci. Technol.*, vol. 51, no. 1, pp. 718–724, Jan. 2017, doi: 10.1021/acs.est.6b03906.

[17] Sandsten J, Weibring P, Edner H, Svanberg S. Real-time gas-correlation imaging employing thermal background radiation. Opt Exp 2000;6(4):92. https://doi.org/10.1364/OE.6.00009210.1364/OE.6.000092.m00110.1364/OE.6.000092.m00210.1364/OE.6.000092.m00310.1364/OE.6.000092.m00410.1364/OE.6.000092.m005.

[18] Wang J, Tchapmi LP, Ravikumar AP, McGuire M, Bell CS, Zimmerle D, et al. Machine vision for natural gas methane emissions detection using an infrared camera. Appl Energy 2020;257:113998. https://doi.org/10.1016/j.apenergy.2019.113998.

[19] M. Gålfalk, G. Olofsson, P. Crill, and D. Bastviken, "Making methane visible," *Nat. Clim. Chang.*, vol. 6, no. 4, 2016, doi: 10.1038/nclimate2877.

[20] N. Hagen *et al.*, "Video-rate spectral imaging of gas leaks in the longwave infrared," in *Chemical, Biological, Radiological, Nuclear, and Explosives (CBRNE) Sensing XIV*, May 2013, vol. 8710, p. 871005, doi: 10.1117/12.2015520.

[21] Hagen N, Kudenov MW. Review of snapshot spectral imaging technologies. Opt Eng 2013;52(9):090901. https://doi.org/10.1117/1.OE.52.9.090901.

[22] Wainner RT, Green BD, Allen MG, White MA, Stafford-Evans J, Naper R. Handheld, battery-powered near-IR TDL sensor for stand-off detection of gas and vapor plumes. Appl Phys B 2002;75(2):249–54. https://doi.org/10.1007/s00340-002-0984-7.

[23] Well BV, Murray S, Hodgkinson J, Pride R, Strzoda R, Gibson G, et al. An open-path, hand-held laser system for the detection of methane gas. J Opt A Pure Appl Opt 2005;7(6):S420–4. https://doi.org/10.1088/1464-4258/7/6/025.

[24] H. R. Simonsen, J. Henningsen, and T. Mogelberg, "Monitoring of molecular species using near-infrared extended cavity diode lasers," in *LEOS Summer Topical Meeting*, 1997, pp. 46–47, doi: 10.1109/leosst.1997.619214.

[25] Frish MB, Wainner RT, Green BD, Stafford-Evans J, Laderer MC, Allen MG. "Progress in reducing size and cost of trace gas analyzers based on tunable diode laser absorption spectroscopy", in *Advanced Environmental. Chemical, and Biological Sensing Technologies II*, Dec. 2004;5586:76. https://doi.org/10.1117/12.580938.

[26] R. T. Wainner, N. F. Aubut, M. C. Laderer, and M. B. Frish, "Scanning, standoff TDLAS leak imaging and quantification," in *Next-Generation Spectroscopic Technologies X*, May 2017, vol. 10210, p. 1021006, doi: 10.1117/12.2264799.

[27] Golston LM, Tao L, Brosy C, Schäfer K, Wolf B, McSpiritt J, et al. Lightweight mid-infrared methane sensor for unmanned aerial systems. Appl Phys B 2017;123(6). https://doi.org/10.1007/s00340-017-6735-6.

[28] Yang S, Talbot R, Frish M, Golston L, Aubut N, Zondlo M, et al. Natural gas fugitive leak detection using an unmanned aerial vehicle: Measurement system description and mass balance approach. Atmosphere (Basel) 2018;9(10):383. https://doi.org/10.3390/atmos9100383.

[29] Baumgartner RA, Byer RL. Continuously tunable ir lidar with applications to remote measurements of SO_2 and CH_4. Appl Opt 1978;17(22):3555. https://doi.org/10.1364/AO.17.003555.

[30] Gardiner T, Helmore J, Innocenti F, Robinson R. Field Validation of Remote Sensing Methane Emission Measurements. Remote Sens. 2017;9(9):956. https://doi.org/10.3390/rs9090956.

[31] Chambers AK, Strosher M, Wootton T, Moncrieff J, McCready P. Direct measurement of fugitive emissions of hydrocarbons from a refinery. J. Air Waste Manag. Assoc. 2008;58(8):1047–56. https://doi.org/10.3155/1047-3289.58.8.1047.

[32] Abshire J, Ramanathan A, Riris H, Mao J, Allan G, Hasselbrack W, et al. remote sensing Airborne Measurements of CO 2 Column Concentration and Range Using a Pulsed Direct-Detection IPDA Lidar. Remote Sens 2011;6(1):443–69. https://doi.org/10.3390/rs6010443.

[33] Innocenti F, Robinson R, Gardiner T, Finlayson A, Connor A. Differential Absorption Lidar (DIAL) Measurements of Landfill Methane Emissions. Remote Sens. 2017;9(9):953. https://doi.org/10.3390/rs9090953.

[34] H. Riris *et al.*, "The challenges of measuring methane from space with a lidar," in *International Conference on Space Optics — ICSO 2018*, 2019, vol. 11180, pp. 829–838, [Online]. Available: https://doi.org/10.1117/12.2535998.

[35] Marshall GF. Risley prism scan patterns. Optical Scan: Des Appl 1999;3787:74–86. https://doi.org/10.1117/12.351658.

[36] Takeuchi N, Sugimoto N, Baba H, Sakurai K. Random modulation cw lidar. Appl Opt 1983;22(9):1382. https://doi.org/10.1364/ao.22.001382.

[37] Ai X, Pérez-Serrano A, Quatrevalet M, Nock RW, Dahnoun N, Ehret G, et al. Analysis of a random modulation single photon counting differential absorption lidar system for space-borne atmospheric CO_2 sensing. Opt. Exp 2016;24(18):21119. https://doi.org/10.1364/OE.24.021119.

[38] Shalom H, Zadok A, Tur M, Legg PJ, Cornwell WD, Andonovic I. On the various time constants of wavelength changes of a DFB laser under direct modulation. IEEE J. Quant Electron 1998;34(10):1816–22. https://doi.org/10.1109/3.720212.

[39] W. H. White *et al.*, "Formation and transport of secondary air pollutants: Ozone and aerosols in the St. Louis urban plume," *Science (80-.).*, vol. 194, no. 4261, pp. 187–189, Oct. 1976, doi: 10.1126/science.959846.

[40] Allan DW. Statistics of atomic frequency standards. Proc. IEEE 1966;54(2):221–30. https://doi.org/10.1109/PROC.1966.4634.

[41] Jongaramrungruang S, Frankenberg C, Matheou G, Thorpe AK, Thompson DR, Kuai Le, et al. Towards accurate methane point-source quantification from high-resolution 2-D plume imagery. Atmos Meas Tech. 2019;12(12):6667–81. https://doi.org/10.5194/amt-12-6667-2019.